Journal of Materials Chemistry A

ROYAL SOCIETY OF CHEMISTRY

PAPER

View Article Online
View Journal | View Issue

Check for updates

Cite this: *J. Mater. Chem. A*, 2025, **13**, 16850

Single iron site catalysts with increased metal-site loading *via* a high-temperature imprinting approach for proton exchange membrane fuel cells†

Xinhong Liang,[abc] Pengwei Zhao,[d] Zhiyuan Gao,[abc] Jiashun Liang,[e] Xiaoxuan Yang,[e] Kai Ao,[abc] Jianwen Zhu,[abc] Yi Mei,[abc] Gang Wu [e] and Yuanzhi Zhu *[abc]

Received 15th February 2025
Accepted 21st April 2025

DOI: 10.1039/d5ta01260k

rsc.li/materials-a

Fe–N–C materials have been widely accepted as the most promising catalysts to replace Pt in future fuel cells. However, the loading of active atomic Fe sites in catalysts remains insufficient (<1.0 wt%) due to Fe agglomeration and carbothermal reduction during the synthesis at elevated heating temperatures (>900 °C). Here, we explored an active-site imprinting approach to convert less active ZnN_x or nitrogen vacancies (V-N_x) into FeN_4. We demonstrated that the reaction barrier of ZnN_4 to FeN_4 (trans-metalation) pathways is significantly lower than that of V-N_4 to FeN_4 (metalation) ones, indicating the importance of forming high-loading ZnN_4 sites first. $FeCl_2$ precursors are preferable over $FeCl_3$ during active-site imprinting despite their relatively high boiling point. Eventually, the high-temperature active-site imprinting strategy based on a vacuum-sealed reaction system enables an Fe–N–C catalyst containing exceptionally high atomic Fe site loading up to 5.65 wt%. The resulting catalyst exhibited encouraging ORR activity and stability in challenging acidic media.

Introduction

Atomically dispersed metal sites (ADMSs)[1,2] have shown significant benefits for energy-conversion related electrocatalytic reactions, including the oxygen reduction reaction (ORR),[3] oxygen evolution reaction (OER),[4,5] hydrogen evolution reaction (HER),[6,7] and CO_2 reduction reaction (CO_2RR).[8] Especially for the ORR[9–12] in challenging acidic electrolytes, nitrogen-coordinated Fe atoms embedded into a carbon support (Fe–N–C) have emerged as the most promising ADMSs among the platinum group metal-free (PGM-free) catalysts.[13,14] These Fe–N–C catalysts have exhibited considerable performance in proton-exchange membrane fuel cells (PEMFCs), and have potential to replace Pt soon.[13,15–17] In particular, over the past decade, significant progress has been made in enhancing the acidic ORR activity of Fe–N–C catalysts by increasing the abundance of atomically dispersed Fe as FeN_4.[17,18] However, most Fe–N–C materials reported to date achieve an Fe content of less than 1 wt% (ref. 19) through conventional high-temperature treatment methods. Adding excess Fe site sources often leads to the clustering of Fe atoms, resulting in inactive aggregates such as metallic iron, iron carbide, and iron nitride, in turn, causing activity decline. This phenomenon is associated with the carbothermal reduction catalyzed by the Fe element at elevated temperatures, described as the dilemma of Fe–N–C catalysts.[20] Therefore, innovative synthetic chemistry and approaches are highly desired to significantly increase Fe site loadings in catalysts for improved mass activity.

Recent studies indicate that decoupling the formation of FeN_4 sites from the high-temperature pyrolysis process is an effective strategy for achieving high-density FeN_4 active sites. This method employs less-noble metals, *e.g.*, Zn[21] or Mg,[22] to induce MN_x sites or protonated nitrogen-vacancy (V-N_x) sites. These sites are then converted into FeN_4 through subsequent metallization (eqn (1)) or trans-metalation reaction (eqn (2)), referred to as active site imprinting methods. Given that Zn and Mg exhibit lower catalytic activity for carbothermal reduction than Fe, this approach enables the attainment of a higher number of FeN_4 sites in catalysts.

$$Fe^{2+} + V\text{-}N_4 \rightarrow Fe^{II}N_4 \quad (1)$$

[a]*Faculty of Chemical Engineering, Kunming University of Science and Technology, Kunming 650500, P. R. China. E-mail: yuanzhi_zhu@kust.edu.cn*

[b]*Yunnan Provincial Key Laboratory of Energy Saving in Phosphorus Chemical Engineering and New Phosphorus Materials, Kunming 650500, P. R. China*

[c]*Yunnan Technological Innovation Center of Phosphorus Resources, Kunming 650600, P. R. China*

[d]*School of Chemical Engineering and Technology, State Key Laboratory of Chemical Engineering, Collaborative Innovation Center of Chemical Science and Engineering, Tianjin University, Tianjin, 300072, China*

[e]*Department of Chemical and Biological Engineering, University at Buffalo, The State University of New York, Buffalo, New York 14260, USA*

† Electronic supplementary information (ESI) available. See DOI: https://doi.org/10.1039/d5ta01260k

$$Fe^{2+} + M^{II}N_4 \rightarrow Fe^{II}N_4 + M^{2+} \quad (2)$$

Fellinger *et al.* pioneered a low-temperature active-site imprinting strategy, in which the initially formed MgN_4 sites were converted into FeN_4 moieties *via* ion exchange using $FeCl_2$ in methanol.[22] However, this method was inefficient for achieving a high density of FeN_4 when using ZnN_4. Furthermore, a more efficient system for ZnN_4-based trans-metalation was developed using $FeCl_3$/LiCl low-temperature molten salt precursors, achieving an atomically dispersed Fe loading of 3.12 wt%.[21] Unlike the trans-metalation mechanism, Stahl *et al.* reported a metallization method involving the exchange of Fe and protons between $FeCl_2$ and V-N_4 with tributyl amine as a promoter.[23] However, the ORR activity of the Fe–N–C catalysts commonly requires activation through acid workup and a second high-temperature treatment, aiming to activate Fe ions adsorbed on the N sites in the form of iron oxide and form active FeN_4 sites.[20]

High-temperature active-site imprinting offers an alternative route to achieve a high density of FeN_4. F. Jaouen *et al.* recently reported a chemical vapor deposition (CVD) method to form Fe–N–C ORR catalysts, proposing that the FeN_4 sites are primarily formed through high-temperature trans-metalation involving the exchange of Fe and Zn between ZnN_4 and $FeCl_3$.[24] Kucernak reported a high FeN_4 loading of 7 wt%, achieved by selective removal of Zn^{2+} ions from V-N_4 prior to metalation,[25] suggesting a metalation-based pathway. However, the reaction pathways during FeN_4 formation remain unclear.

Herein, we reported a high-temperature active-site imprinting method in a closed reaction system with a controlled temperature gradient. Theoretical and experimental research demonstrated that this method can simultaneously utilize ZnN_4 and V-N_4 to form dense FeN_4 sites. We also elucidated a lower reaction barrier of trans-metalation compared to metalation. Additionally, a stoichiometric amount of the Fe precursor is determined during high-temperature active-site imprinting, effectively preventing the Fe–N–C catalyst's deactivation caused by Fe particle agglomeration. The newly obtained Fe–N–C catalyst achieved an exceptional loading of 5.65 wt% atomic Fe in the form of FeN_4 sites, exhibiting considerable ORR performance under acidic conditions.

Results and discussion

High-temperature active-site imprinting involves the reaction between pre-synthesized Zn–N–C and anhydrous iron(II) chloride ($FeCl_2$) or iron(III) chloride ($FeCl_3$), obtaining the corresponding Fe^{II}–N–C or Fe^{III}–N–C samples. This process was conducted in a hermetically sealed silica glass ampoule, exposed to a temperature gradient from 720 to 760 °C (Fig. 1). The temperature gradient was employed to intensify gas-phase disturbance, thereby accelerating the reaction rate. The temperature gradient, fluctuating slightly above and below the boiling point of zinc chloride ($ZnCl_2$) in the hotter and colder zones of the ampoule, would facilitate the separation of the newly formed $ZnCl_2$ from Fe–N–C. The disappearance of $FeCl_2$ and the generation of $ZnCl_2$ (a greyish-white substance) are clearly observed (Fig. S1†). Such a separation is crucial for promoting the trans-metalation reaction.

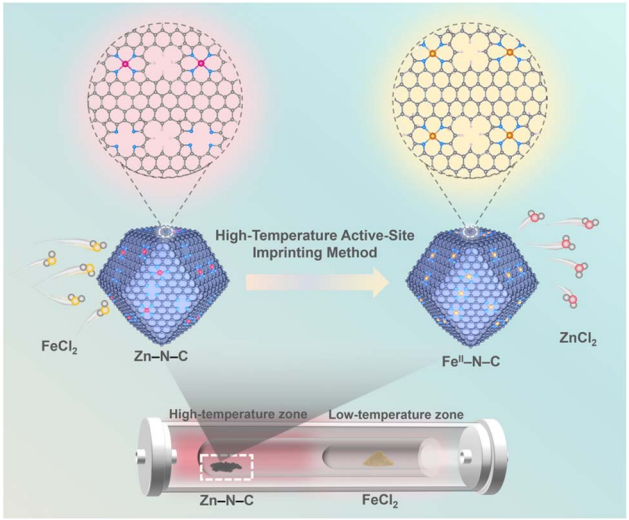

Fig. 1 Schematic illustration of the high-temperature active-site imprinting process.

DFT calculations

Before experimental optimization, a density functional theory (DFT) study was conducted to investigate the reaction barrier associated with the coordination of Fe to either V-N_4 or ZnN_4 sites. According to previous studies,[26–28] we constructed an FeN_4–C_{12} model with a pyrrole-like FeN_4 moiety bridging two adjacent zigzag graphitic edges (Fig. S2†). The corresponding V-N_4 models without Fe atomic centers were also constructed to study the reaction barrier of metalation compared to trans-metalation. We proposed the following reaction steps to delineate the interaction between the Fe resource and the Zn–N–C precursor:

$$FeCl_2 + ZnN_4 \rightarrow FeN_4 + ZnCl_2 \quad (R1)$$

$$FeCl_2 + V\text{-}N_4 + 2H \rightarrow FeN_4 + 2HCl(g) \quad (R2)$$

$$FeCl_3 + ZnN_4 + H \rightarrow FeN_4 + ZnCl_2(g) + HCl \quad (R3)$$

$$FeCl_3 + V\text{-}N_4 + 3H \rightarrow FeN_4 + 3HCl(g) \quad (R4)$$

where the H element comes from the carbon support.

We model the adsorptions of $FeCl_2$ and $FeCl_3$ molecules on ZnN_4 or V-N_4 sites, including the transition state where the V-N_4 sites anchor the Fe–Cl, Zn–Cl, and H–Cl intermediates, as well as the formation of FeN_4 sites (Fig. 2a, b and S2a, b†). The DFT results (Fig. 2c and Table S1†) reveal that the activation energies follow the sequence reaction (R1) (0.14 eV) < reaction (R2) (0.93 eV) < reaction (R3) (1.23 eV) < reaction (R4) (1.82 eV), indicating that $FeCl_2$ is a more favorable precursor compared to $FeCl_3$. The activation barrier for reaction (R1) is significantly lower than that for other reaction pathways, because its translation state

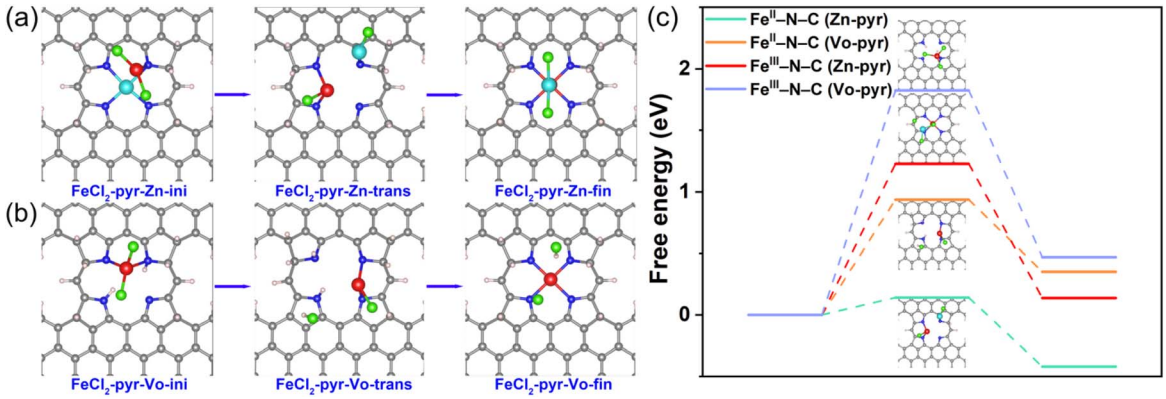

Fig. 2 (a and b) The DFT theoretical calculation model for reactions between (a) $FeCl_2$ and ZnN_4 and (b) $FeCl_2$ + V-N_4 + 2H. (c) Energy diagram for the trans-metalation and metalation reactions, including the transition states; the inset shows the adsorption geometries of various transition states.

does not involve the H atoms from the carbon support. For both $FeCl_2$ and $FeCl_3$, the formation energies of FeN_4 following trans-metalation pathways are lower than that for metalation pathways, suggesting that a higher abundance of ZnN_4 motifs can promote the formation of FeN_4 sites.

Morphology and structure characterization

Based on the DFT calculation, $FeCl_2$ was initially selected as the vapor-phase Fe resource for preparing Fe^{II}–N–C catalysts. To attain a high density of ZnN_4 sites in the Zn–N–C precursor, the pyrolytic temperature was controlled at 900 °C.[29,30] Temperatures exceeding this threshold could significantly induce nitrogen dopants depletion, whereas temperatures below it might lead to insufficient carbonization with poor electrical conductivity.[16] Scanning electron microscope (SEM) images show that the synthesized Fe^{II}–N–C is a regular dodecahedron (Fig. 3a). The transmission electron microscopy (TEM) images show that the as-synthesized Zn–N–C retained the pristine morphology of ZIF-8 with a uniform size of approximately 150 nm (Fig. 3b and S3a, b†). The EDS mapping images of Zn–N–C revealed that only atomically dispersed Zn element was present without other metals (Fig. S3c and d†). In contrast, the presence of the Fe element was apparent in the Fe^{II}–N–C catalyst (Fig. 3d).

The atomic-resolution high-angle annular dark-field scanning TEM (HADDF-STEM) image shows isolated single Fe atoms throughout the Fe^{II}–N–C catalyst without agglomerated metal clusters or particles detected (Fig. 3c). The XRD (Fig. 3e) and Raman (Fig. 3f) results reveal that Zn–N–C and Fe^{II}–N–C exhibit similar diffraction peaks at 25.0° and 43.0° and comparable I_D/I_G values.[31] This indicates that high-temperature active-site imprinting does not change the basic structure of the carbonaceous skeleton. The nitrogen adsorption–desorption isotherms (Fig. 3g) are type I isotherms with limited hysteresis for Zn–N–C and Fe^{II}–N–C, indicating predominant microporous structures. The Brunauer–Emmett–Teller specific surface areas (SSAs) were slightly increased from 1076 $m^2\ g^{-1}$ for Zn–N–C to 1180 $m^2\ g^{-1}$ for Fe^{II}–N–C. Their micropore volumes are 0.761 and 1.047 $cm^3\ g^{-1}$, respectively (Fig. S4†). The increase in SSAs and micropore volumes for Fe^{II}–N–C suggests that vaporized $FeCl_2$ may unblock the channels of the carbon support that are initially not gas-phase accessible in the Zn–N–C precursor. This phenomenon may be attributed to the intercalation effect of $FeCl_2$ into graphitic carbon accompanied by the formation of gaseous $ZnCl_2$.[32]

X-ray photoelectron spectroscopy (XPS) N 1s spectra of Zn–N–C and Fe^{II}–N–C (Fig. 4a) reveal N–H species at 400.68 eV and N–M at 399.7 eV. In comparison, Fe^{II}–N–C preserves similar proportions of N–H and N–M components to Zn–N–C. However, the N–M signal of Fe^{II}–N–C slightly shifts towards a higher bond energy due to the stronger electronic interaction in Fe–N compared to Zn–N. XPS comparison shows a significant decrease in the Zn signal (Fig. S5†) and an increase in the Fe signal in the Fe^{II}–N–C catalyst (Fig. 4c). Owing to the limited penetration depth of XPS, the Zn and Fe contents were further quantified using ICP-OES (Fig. 4b). Fe^{II}–N–C demonstrates a considerably high Fe loading of 5.3 wt%, while the residual Zn content decreases from 3.86 wt% to 0.65 wt%. The increase in the number of Fe atoms exceeds the number of removed Zn atoms, suggesting that the Fe atoms likely occupy unoccupied V-N_4 cavities as well. Therefore, the high-temperature active-site imprinting process can simultaneously utilize ZnN_4 and V-N_4 sites to form dense FeN_4. To further confirm the reaction mechanism, we employed online mass spectrometry to analyze the gas composition from the $FeCl_2$ and Fe^{II}–N–C mixture and the pure $ZnCl_2$ control at elevated temperatures. As depicted in Fig. 4d, distinct signals for Zn and Cl atoms appeared when the heating temperature exceeded ~650 °C. This may be due to $ZnCl_2$ dissociating into Zn and Cl atoms,[33,34] which have lower volatilization temperatures. Additionally, $ZnCl_2$ molecules are prone to condensation before entering the pipeline ahead of the mass spectrometer, thus making them difficult to detect. This result is consistent with the experimental observation of the white $ZnCl_2$ precipitate that appeared in the low-temperature zone of the quartz tube after the reaction (Fig. 1).

X-ray absorption fine structure (XAFS) analyses, comprising X-ray absorption near-edge structure (XANES) and extended X-ray absorption fine structure (EXAFS), were conducted to investigate the coordination environment and valence state of

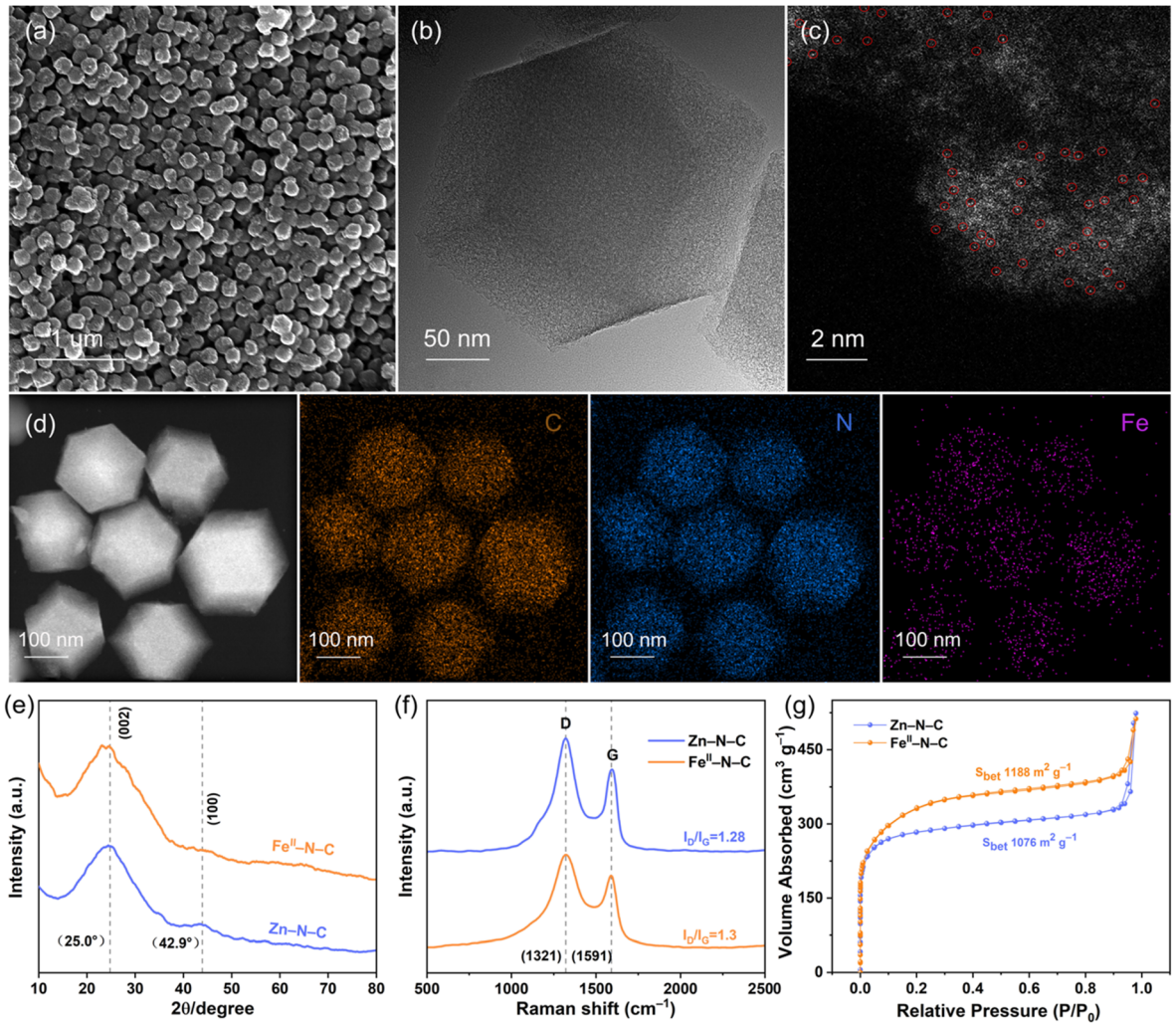

Fig. 3 (a) SEM image of Fe^{II}–N–C. (b and d) TEM image and corresponding EDS mapping of Fe^{II}–N–C. (c) Atomic-resolution HADDF-STEM image of Fe^{II}–N–C. (e) XRD pattern of Fe^{II}–N–C. (f) Raman spectrum of Fe^{II}–N–C. (g) N_2 isothermal desorption curve of Zn–N–C and Fe^{II}–N–C.

the atomically dispersed metal species.[35] The Zn K-edge XANES spectra (Fig. 5a) reveal that the near-edge absorption energy of Zn–N–C is located between those of Zn foil and ZnO, similar to that of Zn phthalocyanine (ZnPc), suggesting the presence of cationic Zn states in the Zn–N–C precursor. The Fourier-transform (FT) k^3-weighted EXAFS spectra (FT-EXAFS) of Zn–N–C display a distinct peak at approximately 1.5 Å (Fig. 5b), likely ascribed to the Zn–N scattering path originating from atomically dispersed Zn sites. The coordination number and bond length between Zn and N are estimated to be around 4 and 2.01 Å, respectively (Fig. S6 and Table S2†).

The Fe K-edge XANES spectra (Fig. 5d) reveal that the absorption edge position of the Fe^{II}–N–C catalyst falls between that of FePc and Fe_2O_3, indicating that the valence state of Fe species ranges from +2 to +3. The Fe FT-EXAFS curve (Fig. 5e) of Fe^{II}–N–C indicates a scattering path at similar radial distances to that of FePc, likely containing an analogous pyrrolic N coordination environment. A primary peak of Fe^{II}–N–C appears at 1.6 Å, representing the first Fe–N or Fe–O coordination. Notably, there is no Fe–Fe scattering peak at ~2.2 Å in the Fe^{II}–N–C catalyst.[36] The wavelet transformed (WT) EXAFS spectra discern the contributions of each pathway not only in *R*-space but also in *k*-space. The k^3-weighted WT-EXAFS spectra (Fig. 5c) for Fe^{II}–N–C exhibit a contour profile in *k*-space aligns well with the FePc pattern, albeit with a subtle shift in the contour intensity maximum exhibits partical characteristics of Fe_2O_3. Therefore, the coexistence of Fe–N and Fe–O bonds within the Fe^{II}–N–C catalyst is likely.

Quantitative structural configuration information for these samples was extracted by least-squares EXAFS curve fitting analyses (Fig. S7 and Table S2†). The analysis suggests that the primary coordination shell of Fe^{II}–N–C is a blend of Fe–N and Fe–O coordination paths, with Fe coordination numbers of 4.0 (N) and 2 (O), respectively. This result implies that the central Fe sites in Fe^{II}–N–C possessed a FeN_4O_2 configuration, *i.e.*, near square planar FeN_4 moieties with two axial oxygen atoms. Recent studies underscore the significance of gas- and proton-accessible FeN_4O_2 sites for enhanced ORR activity, alongside the FeN_4 sites whose oxidation and spin states remain unaltered at varying electrochemical potentials.[24] The cyclic voltammetry (CV) curve in O_2/

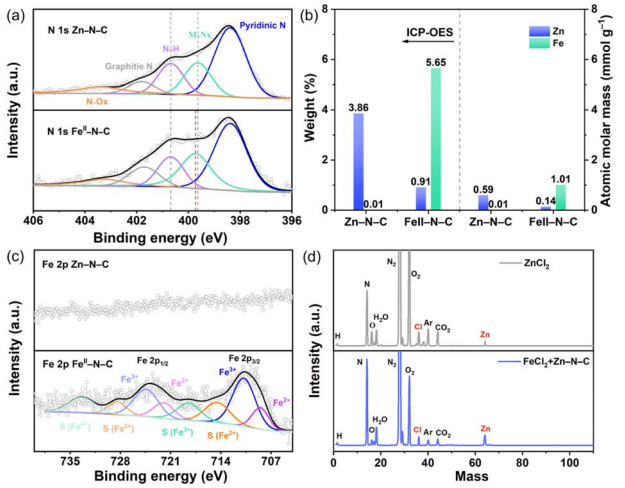

Fig. 4 (a) High-resolution N 1s XPS spectra of Zn–N–C and Fe^{II}–N–C. (b) The histogram reveals the weight fraction (wt%) of Zn and Fe for Zn–N–C and Fe^{II}–N–C detected by ICP-OES (left) and the corresponding values converted to atomic number per gram of the sample (mmol g^{-1}) (right). (c) High-resolution Fe 2p XPS spectra of Zn–N–C and Fe^{II}–N–C. (d) Mass spectrum analysis of the reaction process ($FeCl_2$ and ZnN_4).

N_2-saturated electrolyte demonstrates that Fe^{II}–N–C undergoes a reversible Fe^{III}/Fe^{II} redox transition at ~0.66 V, predominantly attributable to the redox-active Fe sites (Fig. S8†).

Catalyst activity and stability

The ORR activity of the Fe^{II}–N–C, Fe^{III}–N–C, Zn–N–C, and Pt/C catalysts was evaluated in 0.1 M $HClO_4$ electrolyte. As depicted in Fig. 6a, the Fe^{II}–N–C catalyst exhibits a half-wave potential ($E_{1/2}$) of 0.86 V and a kinetic current density (j_k) of 60.8 mA cm^{-2} at 0.8 V, and significantly outperforms the Zn–N–C precursor. The calculated turnover frequency (TOF) values for Fe^{II}–N–C at 0.80 and 0.85 V were 0.84 and 7.7 e per site per s, respectively (Fig. S9†). The *in situ* nitrite stripping technique was employed to quantify the active site density (SD).[37,38] LSV curves were recorded in oxygen-saturated solutions under three conditions: pre-poisoning, poisoned, and recovered states. The stripping process involves cyclic voltammetry in argon-saturated solution, where a reduction peak appears due to NO reduction to ammonia, linking the stripping charge to the NO molecule quantity and consequently to Fe–N_x site density in the catalyst. A pronounced nitrite reduction peak emerged in Fe^{II}–N–C in the poisoned CV cycles, implying that the active sites synthesized by high-temperature active-site imprinting are accessible to gas and protons. The total amount of charge associated with the NO stripping peak of Fe^{II}–N–C was quantified as 20.49 C g^{-1} (Fig. 6b), corresponding to an SD value of 4.27×10^{19} sites per g. The TOF value for the Fe^{II}–N–C catalyst at 0.85 V was evaluated to be 0.84 e per site per s. These values are comparable to those of the state-of-the-art Fe–N–C catalysts in Table S3,† indicating the high loading and intrinsic activity of the Fe sites in Fe^{II}–N–C. The Tafel slope of the ORR over the Fe^{II}–N–C catalyst is 87 mV dec^{-1}, indicating favorable ORR kinetics (Fig. S10†). Evaluated by the rotating ring-disc electrode (RRDE) technique, the average electron transfer number of Fe^{II}–N–C is 3.94 (Fig. S11†) with an H_2O_2 yield below 4%, which is consistent with the linear fitting result from the K–L equation (Fig. S12†). After 5000 potential cycles, no ORR activity loss was observed (Fig. S13†), and chronoamperometric measurements at 0.4 V demonstrated 84% current retention after a 40000 s test (Fig. S14†), indicating good ORR stability of the Fe^{II}–N–C catalyst in aqueous acidic electrolytes.

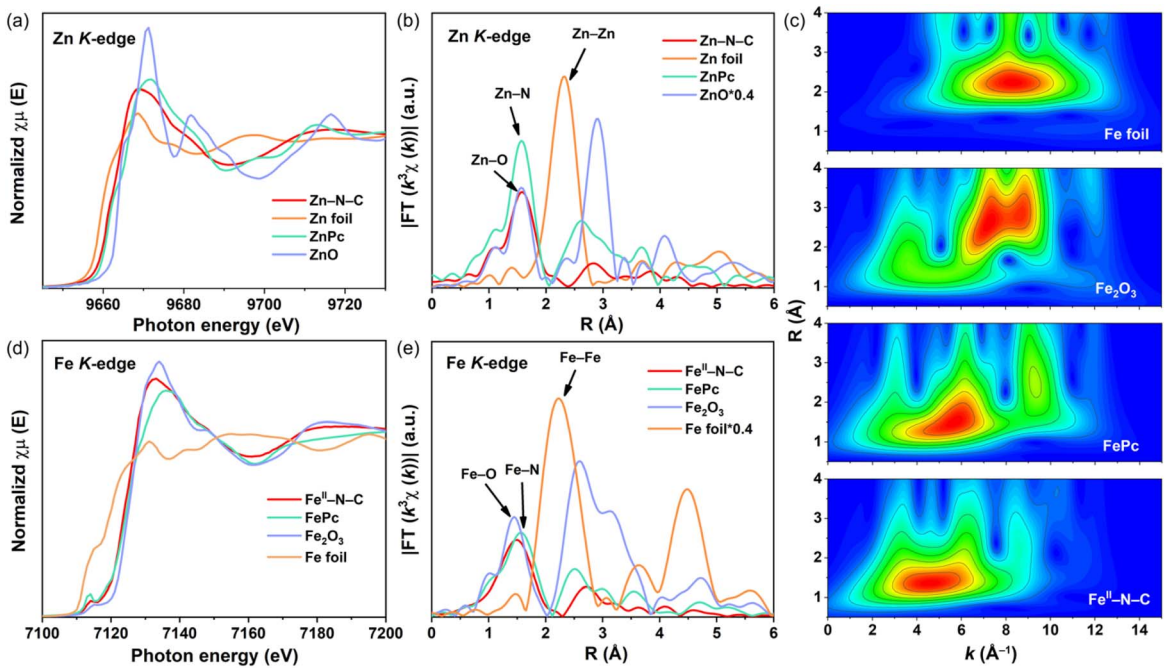

Fig. 5 (a) Zn K-edge XANES spectra, and (b) FT-EXAFS spectra of Zn–N–C and corresponding control samples (Zn foil, ZnPc, and ZnO). (d) Fe K-edge XANES spectra, (e) FT-EXAFS spectra, and (c) WT-EXAFS images of Fe^{II}–N–C and corresponding control samples (FePc, Fe_2O_3, and Fe foil).

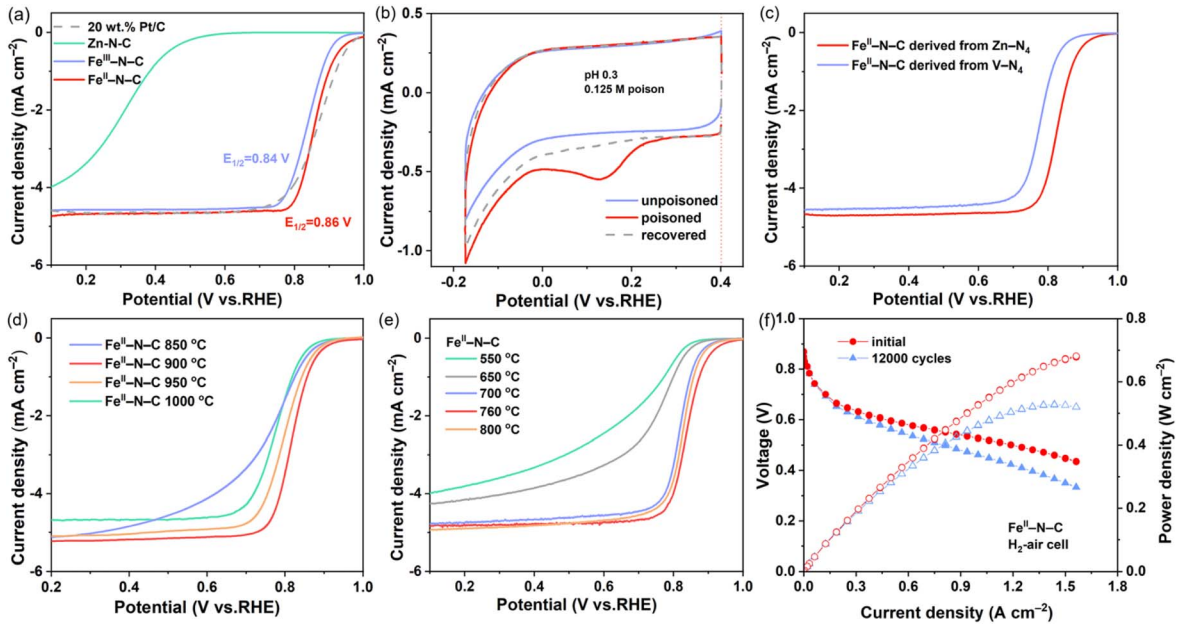

Fig. 6 (a) ORR polarization curves of Fe^{II}–N–C, Fe^{III}–N–C, Zn–N–C, and Pt/C catalysts in 0.1 M $HClO_4$ electrolyte. (b) CV curves of Fe^{II}–N–C before and after nitrite adsorption in the nitrite reductive stripping region. (c) ORR polarization curves of Fe^{II}–N–C from Zn–N–C and V–N–C precursors at 0.1 M $HC1O_4$. (d) ORR polarization curves of Fe^{II}–N–C derived from Zn–N–C precursors at various pyrolytic temperatures. (e) ORR polarization curves of Fe^{II}–N–C synthesized at different active-site imprinting temperatures. (f) Polarization and power density curves of the optimal Fe^{II}–N–C catalyst before and after 12 000 cycles under H_2–Air conditions. Test conditions: the anode loading is 0.1 mg cm^{-2}, the cathode loading is 4.0 mg cm^{-2}, the relative humidity is 100%, and the battery temperature is 80 °C.

To investigate the impact of the ZnN_4 sites within the Zn–N–C precursor on the ORR activity of Fe^{II}–N–C, the ZnN_4 sites were converted into V-N_4 through an intense acidic washing treatment. Under identical active site imprinting conditions, the $E_{1/2}$ of the control sample decreased obviously by 50 mV (Fig. 6c), implying that trans-metalation facilitates the formation of more FeN_4 sites than metalation. We further synthesized Zn–N–C precursors with varying Zn contents by pyrolyzing ZIF-8 at different temperatures. As depicted in Fig. 6d, the ORR activity of Fe^{II}–N–C (*T*) catalysts, where *T* represents the pyrolysis temperature of the Zn–N–C catalyst *via* high-temperature active-site imprinting, follows the order Fe^{II}–N–C (900 °C) > Fe^{II}–N–C (950 °C) > Fe^{II}–N–C (1000 °C) > Fe^{II}–N–C (850 °C). This result reveals that the Zn content is closely related to the ORR activity, as the trans-metalation pathway has a lower reaction barrier than the metallization pathway. Meanwhile, pyrolysis temperatures lower than 900 °C lead to higher Zn content but a significant decrease in conductivity. Conversely, exceeding 900 °C results in the loss of N content, leading to fewer ZnN_4 sites. Both extreme heating temperatures lead to a decrease in FeN_4 density. To determine the optimal Fe loading, we conducted a series of comparative experiments using different mass ratios of the Fe source to Zn–N–C precursor, corresponding to Fe^{II}–N–C catalysts with 5%, 15%, 25%, and 35% Fe contents. The ORR activity initially improves with increasing Fe content, reaching an optimum at 15%, and then declines with further increases (Fig. S15†).

We further investigate the impact of reaction temperatures of the active-site imprinting process on the ORR performance of the Fe^{II}–N–C (900 °C) catalyst. As shown in Fig. 6e, a reaction temperature around the boiling point of $ZnCl_2$ (760 °C) leads to the best ORR activity, and the temperature gradient facilitates the activity enhancement (Fig. S16†).

Since $FeCl_3$ has a lower boiling point than $FeCl_2$, we further explored using $FeCl_3$ as a Fe resource (denoted as Fe^{III}–N–C) for high-temperature active-site imprinting. Interestingly, the Fe^{III}–N–C catalyst exhibited relatively lower ORR activity than the Fe^{II}–N–C catalyst (Fig. 6a), despite the easier volatilization of $FeCl_3$ compared to $FeCl_2$. This result is consistent with the DFT conclusions, indicating that $FeCl_2$ has a lower reaction barrier for both metalation and trans-metalation. Moreover, $FeCl_2$ is more stable, whereas $FeCl_3$ is prone to decomposition, forming chlorine (Cl) to poison the FeN_4 sites by forming Fe–Cl coordination. Besides, even at temperatures lower than the boiling point of $FeCl_2$, the reaction can still proceed because the closed vacuum system can reduce the vapor pressure, and the temperature gradient also promotes the gaseous reaction.

Fuel cell testing

To evaluate the Fe^{II}–N–C catalyst in a practical PEMFC, the catalyst was incorporated into membrane electrode assemblies (MEAs) and investigated under fuel cell operating conditions. As shown in Fig. S17,† the Fe^{II}–N–C cathode exhibited an open-circuit voltage (OCV) of 0.92 V and a peak power density of 1.29 W cm^{-2} under 1.8 bar H_2–O_2 conditions. Under more practical H_2–air conditions, the peak power density is still around 0.68 W cm^{-2} (Fig. 6f). After an accelerated stress test (AST) using 12 000 voltage cycles, the Fe^{II}–N–C cathode only lost about 29% and 24% under H_2–O_2 and H_2–air conditions,

respectively, comparable to most reported Fe–N–C catalysts due to the possible demetallation in harsh fuel cell environments.[39,40] Significant efforts are still needed to simultaneously improve fuel cell performance and durability, which remains a grand challenge in the field.

Conclusions

In summary, we have developed a high-temperature active-site imprinting method to effectively synthesize Fe–N–C catalysts with significantly increased atomic FeN_4 site loading. Theoretical and experimental research elucidates that the reaction mechanism involves the trans-metalation between $FeCl_2$ and ZnN_4 and the direct metalation between $FeCl_2$ and V-N_4. The reaction barrier for trans-metalation is lower than that for direct metalation, suggesting that more ZnN_4 in the Zn–N–C precursor is essential for achieving high loading of FeN_4 sites. $FeCl_2$ is a more suitable Fe resource for this process than $FeCl_3$ due to the reduced energy barrier during the imprinting process. In particular, the vacuum-sealed reaction system enables the use of high boiling point $FeCl_2$ as a precursor to trigger the active-site imprinting reaction. Only a stoichiometric amount of Fe precursor is required, preventing the deactivation of the Fe–N–C catalyst due to the formation of Fe agglomeration. As the gasified $FeCl_2$ and $ZnCl_2$ may open the channels of the carbon support, the FeN_4 sites are easily accessible to both gas and protons during the ORR. The optimal Fe–N–C catalyst achieved a high FeN_4 loading of 5.65 wt%, exhibiting high ORR performance under acidic conditions, as evidenced by the RDE technique in acidic solution and MEA tests under PEMFC conditions. This study provides insight into the formation mechanism of high-loading FeN_4 sites *via* the ZnN_4-rich Zn–N–C precursor using effective high-temperature imprinting.

Experimental

Preparation of Zn–N–C precursors

4.7 g of zinc nitrate hexahydrate was mixed with 100 mL of methanol and 100 mL of water. Simultaneously, 10.02 g of 2-methylimidazole was dissolved in 100 mL of methanol. The methanol solution containing zinc nitrate hexahydrate was then poured into the methanol solution containing 2-methylimidazole and mixed thoroughly, followed by stirring for three hours.[41] After ceasing stirring, the mixture was allowed to stand for 3 hours, and then centrifuged, and the resultant white product was washed several times with methanol. The obtained ZIF-8 powder was then heat-treated in a tube furnace at a heating rate of 3 °C per minute up to 900 °C for 3 hours. The pyrolyzed product underwent treatment in a 0.5 M H_2SO_4 solution at 80 °C for 8 hours to remove excess Zn nanoparticles, followed by repeated washing with water and ethanol, and then drying.

Preparation of Fe^{II}–N–C

A specific ratio (15 wt%) of the Zn–N–C material and ferrous chloride were enclosed in a quartz tube under vacuum conditions, ensuring that the ferrous chloride powder did not directly come into contact with the Zn–N–C powder. The tube was then subjected to pyrolysis at 760 °C in the high-temperature zone and 730 °C in the low-temperature zone for 10 hours. The high-temperature zone is set at 760 °C because this temperature is slightly higher than the vaporization temperature of $ZnCl_2$ (732 °C), ensuring that the formed $ZnCl_2$ will not deposit on the Fe–N–C surface. Meanwhile, the temperature in the low-temperature zone is 730 °C, which facilitates the deposition of $ZnCl_2$, thus enabling its separation from Fe–N–C. After the active-site imprinting reaction, the resulting sample was washed with ethanol and deionized water to yield the Fe^{II}–N–C catalyst. Similarly, $FeCl_3$ precursors were also used for the high-temperature imprinting synthesis under identical procedures and conditions.

XAS characterization

X-ray Absorption Spectroscopy (XAS) was conducted at the Zn K-edge (9659 eV) and Fe K-edge (7112 eV) at the 1W1B beamline of the Beijing Synchrotron Radiation Facility (BSRF). Using a Si (111) double-crystal monochromator, the Zn SAC and Fe SAC data were acquired in the transmission mode and fluorescence mode using a Lytle detector under ambient conditions, respectively.[42] For energy calibration, Zn and Fe foil were tested, and the energy of the most substantial peak of the first-order derivative of its X-ray absorption near edge structure (XANES) was found to be 9659 and 7112 eV, respectively.

The raw data were processed and analyzed using the Demeter software package (including Athena and Artemis software).[43] A linear function was subtracted from the pre-edge region. Then, the edge jump was normalized using Athena software. The $\chi(k)$ data were isolated by subtracting a smooth, third-order polynomial approximating the absorption background of an isolated atom. The k^3-weighted and k^2-weighted $\chi(k)$ data were Fourier-transformed after applying a Hanning window function ($\Delta k = 1$) to extract the EXAFS for Zn and Fe elements, respectively. The global amplitude reduction factor ($S_0{}^2$), coordination numbers (N), distances to the scattering atoms (R), and the Debye–Waller factor (σ^2) were obtained by non-linear least-squares refinement of the EXAFS equation of the Fourier-transformed data in R-space, using Artemis software. The detailed fitting parameters are shown in Table S1.†

Electrochemical evaluations

The catalyst ink was prepared by uniformly dispersing 5 mg of catalyst in 1000 μL mixed solvent (volume ratio of ethanol to 5 wt% perfluorosulfonic acid resin is 99 : 1), and the test equipment was a rotating disk electrode. The ink prepared by using 20 μL catalyst was dropped onto the disk electrode dried in air, and the thin film electrode was evaluated by using an electrochemical workstation. A Pt mesh electrode and Ag/AgCl electrode were used as counter and reference electrodes, respectively. All potentials are related to the reversible hydrogen electrode (RHE). In an Ar-saturated 0.1 M $HClO_4$ solution, 20 cycles of CV cleaning were performed in the potential range of 0 to 1.2 V at 100 mV s^{-1}, and then a stable CV curve was obtained in the same potential range at 50 mV s^{-1}. The ORR

performance was measured at 1600 rpm in an O_2-saturated 0.1 M $HClO_4$ solution. Linear sweep voltammetry was performed on Zn–N–C and Fe^{II}–N–C in the potential range of −0.2 V to 0.9 V at a 5 mV s^{-1} scan rate. To test the durability of Fe^{II}–N–C, the steady-state current of 5000 CV cycles was recorded in the voltage range of 0.33–0.73 V. The LSV curves before and after the cycle were compared.

Fuel-cell testing

The homogeneous suspension of the Fe^{II}–N–C catalyst was prepared in a solvent mixture consisting of isopropanol, water, and a 5 wt% Nafion dispersion. The volumetric ratio of alcohol to water was adjusted to 1 : 1, with the mass of the perfluorosulfonic acid resin solution constituting 50% of the total catalyst mass. After a 20 minute wet milling process with isopropanol solution, water, additional isopropanol, and a 5 wt% Nafion™ solution were added in accordance with the predetermined blending ratio. The resulting mixture was then uniformly dispersed *via* ultrasonication and sprayed onto a Gas Diffusion Layer (GDL) until a cathode catalyst loading of 4.0 mg cm^{-2} was achieved. For the anode, a Pt/C-coated GDL with a Pt loading of 0.1 mg cm^{-2} was used. To create the Membrane Electrode Assembly (MEA), two Gas Diffusion Layers (GDLs) were aligned on either side of a Nafion membrane and thermally pressed for 120 s at 130 °C under a pressure of 3.0 bar.

The performance of the MEA, which had an active area of 4 cm^2, was rigorously evaluated in a fuel cell setup. The operational conditions during the test maintained the battery temperature and Relative Humidity (RH) at 100%, respectively. Before the performance evaluation, the Fe^{II}–N–C cathode underwent an activation phase at a fixed voltage of 0.5 V in an H_2/O_2 environment for 20 minutes. The current density progressively increased during this time until it stabilized at a maximum value. The cathode and anode were supplied with H_2 and O_2 at flow rates of 300 and 800 mL min^{-1}, respectively, both under a back pressure of 1.8 bar. Polarization curves were recorded under these specified conditions. The Fe^{II}–N–C cathode was subjected to durability testing, square-wave potential cycling at 0.6 and 0.92 V with each potential applied for 3 s, following the DOE protocol for evaluating the dura.

Electron transfer number and hydrogen peroxide yield

The electron transfer number from the RDE test was calculated from the Koutecky–Levich equation:[10,44]

$$\frac{1}{J} = \frac{1}{J_k} + \frac{1}{J_L} = \frac{1}{B\omega^{\frac{1}{2}}} + \frac{1}{J_k}$$

where ω is the rotation rate applied in the test. Current density (J) and kinetic current density (J_k) were determined from the steady-state polarization curves. The constant B was calculated from the above equation (diffusion coefficient of O_2 is 1.93 × 10^{-5} cm^2 s^{-1}; the kinetic viscosity ν equals 1.009 × 10^{-2} cm^2 s^{-1}; the concentration of O_2 in the electrolyte is 1.26 × 10^{-3} mol L^{-1}; and F and A are the Faraday constant and the electrode's geometric area (0.19625 cm^2), respectively).

The rotating ring disk electrode (RRDE) test was applied to measure the hydrogen peroxide yield (H_2O_2%) and the electron transfer number (n). During the test, polarization curves were recorded by scanning the disk electrode with a rate of 1 mV s^{-1} in the voltage range of 1.0–0.125 V, where the ring electrode voltage was 1.20 V. H_2O_2 yields are determined by using the following equations:[45]

$$H_2O_2\% = \frac{200I_r}{I_dN + I_r}$$

$$n = \frac{4I_dN}{I_dN + I_r}$$

The currents associated with both the disk (denoted as I_d) and the ring (denoted as I_r) electrodes can be directly extracted from the polarization curves obtained during the experiments. The collection efficiency, symbolized as N, is established to have a value of 0.37. All the electrochemical measurements were performed at room temperature.

Nitrite stripping technique for determining active site density[46]

The nitric oxide (NO) stripping technique employs a classical three-electrode setup, utilizing 0.5 M H_2SO_4 as the electrolyte. The selection of this medium was based on the proposer's rationale that it represents an optimal compromise, emulating the conditions of an acidic measurement while simultaneously providing an adequate potential window to facilitate the observation of NO stripping devoid of interference from hydrogen evolution.[47] LSVs are recorded in an oxygen-saturated solution before poisoning, after poisoning, and after stripping. The stripping procedure is simple cyclic voltammetry (in an oxygen-free solution) where a reductive peak appears because of the reduction of NO to ammonia, which makes the stripping charge linked to the amount of NO molecules and so to the number of Fe^{II}–N–C sites in the material according to the formula:

$$\text{MSD}\ \ [\text{mol per sites per g}] = \frac{Q_{\text{strip}}\ \ [\text{C g}^{-1}]}{n_{\text{strip}}\ F\ \ [\text{C mol}^{-1}]} = \frac{\text{SD}\ \ [\text{site per g}]}{N_A\ \ [\text{mol}^{-1}]}$$

where n_{strip} is the number of electrons associated with the reduction of one adsorbed nitrosyl per site to NH_3 (or more precisely to NH_4^+), which is quantitatively defined as 5.[48] By extracting the difference in kinetic current J_k at 0.8 V/0.85 V *versus* RHE, the mean TOF of all different nitrite sensitive active sites with respect to electrons can be obtained *via*:[49]w

$$\text{TOF} = \frac{J_kA}{\left(\frac{m_{Fe}}{M_{Fe}}\right)N_A} = \frac{J_kA}{\left(\frac{LAW_{Fe}}{M_{Fe}}\right)N_A} = \frac{J_kM_{Fe}}{LN_AW_{Fe}}$$

here J_k is the mass transfer corrected kinetic current density at 0.8 V/0.85 V. A is the electrode area. m_{Fe} is the mass loading of

Fe on the electrode. M_{Fe} is the molar mass of Fe ($M_{Fe} = 55.85$ g mol^{-1}). N is Avogadro's number ($N = 6.02 \times 10^{23}$ mol^{-1}). L is the catalyst loading on the electrode ($L = 0.27$ mg cm^{-2}). W_{Fe} is the mass fraction of Fe in the catalyst from ICP-OES analysis ($W_{Fe} =$ 5.65 wt%).

Data availability

All experimental and characterization data are available in the ESI.†

Author contributions

Xinhong Liang and Pengwei Zhao completed the experimental and theoretical calculation work of this study. Zhiyuan Gao, Jiashun Liang, Xiaoxuan Yang, Kai Ao and Jianwen Zhu contributed to the experimental design and investigation. Yi Mei contributed to the experimental design. Yuanzhi Zhu and Gang Wu were responsible for experimental design, supervision and writing, while Yuanzhi Zhu was responsible for reviewing, editing, and funding acquisition.

Conflicts of interest

There are no conflicts to declare.

Acknowledgements

Y. Z. acknowledges financial support from the Applied Basic Research Program of Yunnan Province (202301AT070796), Yunnan Major Scientific and Technological Projects (No. 202402AF080004), and Analysis and Testing Foundation of Kunming University of Science and Technology. G. W. is thankful for the support from the University at Buffalo, SUNY.

Notes and references

1 Z. Liang, C. Qu, D. Xia, R. Zou and Q. Xu, *Angew Chem. Int. Ed. Engl.*, 2018, **57**, 9604–9633.
2 G. Wu and P. Zelenay, *Nat. Rev. Mater.*, 2024, **9**, 643.
3 H. T. Chung, D. A. Cullen, D. Higgins, B. T. Sneed, E. F. Holby, K. L. More and P. Zelenay, *Science*, 2017, **357**, 479–484.
4 H. Li, J. Wang, R. Qi, Y. Hu, J. Zhang, H. Zhao, J. Zhang and Y. Zhao, *Appl. Catal., B*, 2021, **285**, 119778.
5 Y. Qi, T. Li, Y. Hu, J. Xiang, W. Shao, W. Chen, X. Mu, S. Liu, C. Chen, M. Yu and S. Mu, *Chem. Res. Chin. Univ.*, 2022, **38**, 1282–1286.
6 Y. Lei, Y. Wang, Y. Liu, C. Song, Q. Li, D. Wang and Y. Li, *Angew Chem. Int. Ed. Engl.*, 2020, **59**, 20794–20812.
7 F. Ullah, M. A. Gilani, M. Imran, K. Ayub and T. Mahmood, *Phys. Scr.*, 2023, **98**, 115308.
8 C. S. Hsu, J. Wang, Y. C. Chu, J. H. Chen, C. Y. Chien, K. H. Lin, L. D. Tsai, H. C. Chen, Y. F. Liao, N. Hiraoka, Y. C. Cheng and H. M. Chen, *Nat. Commun.*, 2023, **14**, 5245.
9 Z. Wei, Y. Ren, J. Sokolowski, X. Zhu and G. Wu, *InfoMat*, 2020, **2**, 483–508.
10 F. Xiao, G.-L. Xu, C.-J. Sun, M. Xu, W. Wen, Q. Wang, M. Gu, S. Zhu, Y. Li, Z. Wei, X. Pan, J. Wang, K. Amine and M. Shao, *Nano Energy*, 2019, **61**, 60–68.
11 Y. Wu, X. Li, K. Hua, X. Duan, R. Ding, Z. Rui, F. Cao, M. Yuan, J. Li and J. Liu, *Small*, 2023, **19**, 2207671.
12 K. Liu, J. Fu, Y. Lin, T. Luo, G. Ni, H. Li, Z. Lin and M. Liu, *Nat. Commun.*, 2022, **13**, 2075.
13 R. Peng, Z. Zhao, H. Sun, Y. Yang, T. Song, Y. Yang, J. Shao, H. Jin, H. Sun and Z. Zhao, *Chin. J. Chem.*, 2023, **41**, 710–724.
14 Y. Zhou, R. Lu, X. Tao, Z. Qiu, G. Chen, J. Yang, Y. Zhao, X. Feng and K. Mullen, *J. Am. Chem. Soc.*, 2023, **145**, 3647–3655.
15 Y. He, X. Yang, Y. Li, L. Liu, S. Guo, C. Shu, F. Liu, Y. Liu, Q. Tan and G. Wu, *ACS Catal.*, 2022, **12**, 1216–1227.
16 H. Zhang, S. Hwang, M. Wang, Z. Feng, S. Karakalos, L. Luo, Z. Qiao, X. Xie, C. Wang, D. Su, Y. Shao and G. Wu, *J. Am. Chem. Soc.*, 2017, **139**, 14143–14149.
17 S. W. Liu, C. Z. Li, M. J. Zachman, Y. C. Zeng, H. R. Yu, B. Y. Li, M. Y. Wang, J. Braaten, J. W. Liu, H. M. Meyer, M. Lucero, A. J. Kropf, E. E. Alp, Q. Gong, Q. R. Shi, Z. X. Feng, H. Xu, G. F. Wang, D. J. Myers, J. Xie, D. A. Cullen, S. Litster and G. Wu, *Nat. Energy*, 2022, **7**, 652–663.
18 Q. Liu, X. Liu, L. Zheng and J. Shui, *Angew. Chem., Int. Ed.*, 2018, **57**, 1204–1208.
19 D. Wang, P. Yi, L. Wang, L. Zhang, H. Li, M. Lu, X. Xie, L. Huang and W. Huang, *Front. Chem.*, 2019, **7**, 21.
20 D. Menga, J. L. Low, Y. S. Li, I. Arcon, B. Koyuturk, F. Wagner, F. Ruiz-Zepeda, M. Gaberscek, B. Paulus and T. P. Fellinger, *J. Am. Chem. Soc.*, 2021, **143**, 18010–18019.
21 D. Menga, F. Ruiz-Zepeda, L. Moriau, M. Šala, F. Wagner, B. Koyutürk, M. Bele, U. Petek, N. Hodnik, M. Gaberščček and T. P. Fellinger, *Adv. Energy Mater.*, 2019, **9**, 1902412.
22 A. Mehmood, J. Pampel, G. Ali, H. Y. Ha, F. Ruiz-Zepeda and T. P. Fellinger, *Adv. Energy Mater.*, 2017, **8**, 1701771.
23 J. S. Bates, F. Khamespanah, D. A. Cullen, A. A. Al-Omari, M. N. Hopkins, J. J. Martinez, T. W. Root and S. S. Stahl, *J. Am. Chem. Soc.*, 2022, **144**, 18797–18802.
24 L. Jiao, J. Li, L. L. Richard, Q. Sun, T. Stracensky, E. Liu, M. T. Sougrati, Z. Zhao, F. Yang, S. Zhong, H. Xu, S. Mukerjee, Y. Huang, D. A. Cullen, J. H. Park, M. Ferrandon, D. J. Myers, F. Jaouen and Q. Jia, *Nat. Mater.*, 2021, **20**, 1385–1391.
25 A. Mehmood, M. Gong, F. Jaouen, A. Roy, A. Zitolo, A. Khan, M.-T. Sougrati, M. Primbs, A. M. Bonastre, D. Fongalland, G. Drazic, P. Strasser and A. Kucernak, *Nat. Catal.*, 2022, **5**, 311–323.
26 Y. Zeng, C. Li, B. Li, J. Liang, M. J. Zachman, D. A. Cullen, R. P. Hermann, E. E. Alp, B. Lavina, S. Karakalos, M. Lucero, B. Zhang, M. Wang, Z. Feng, G. Wang, J. Xie, D. J. Myers, J.-P. Dodelet and G. Wu, *Nat. Catal.*, 2023, **6**, 1215–1227.
27 W. Chen, J. Ouyang, H. Liu, M. Chen, K. Zeng, J. Sheng, Z. Liu, Y. Han, L. Wang, J. Li, L. Deng, Y.-N. Liu and S. Guo, *Adv. Mater.*, 2017, **29**, 1603864.
28 H. Zhang, H. T. Chung, D. A. Cullen, S. Wagner, U. I. Kramm, K. L. More, P. Zelenay and G. Wu, *Energy Environ. Sci.*, 2019, **12**, 2548–2558.

29 S. Ding, J. A. Barr, Q. Shi, Y. Zeng, P. Tieu, Z. Lyu, L. Fang, T. Li, X. Pan, S. P. Beckman, D. Du, H. Lin, J. C. Li, G. Wu and Y. Lin, *ACS Nano*, 2022, **16**, 15165–15174.
30 X. Zhao, X. Yang, M. Wang, S. Hwang, S. Karakalos, M. Chen, Z. Qiao, L. Wang, B. Liu, Q. Ma, D. A. Cullen, D. Su, H. Yang, H.-Y. Zang, Z. Feng and G. Wu, *Appl. Catal., B*, 2020, **279**, 119400.
31 Y. Wang, D. C. Alsmeyer and R. L. McCreery, *Chem. Mater.*, 2002, **2**, 557–563.
32 Z. Wang and M. J. C. Inagaki, *Carbon*, 1991, **29**, 423–427.
33 T. L. Charlton and R. G. Cavell, *Inorg. Chem.*, 2002, **6**, 2204–2208.
34 D. L. Hildenbrand, K. H. Lau and J. W. Roos, *J. Chem. Phys.*, 1999, **111**, 1337–1338.
35 J. G. Parsons, M. V. Aldrich and J. L. Gardea-Torresdey, *Appl. Spectrosc. Rev.*, 2002, **37**, 187–222.
36 M. Xiao, J. Zhu, L. Ma, Z. Jin, J. Ge, X. Deng, Y. Hou, Q. He, J. Li, Q. Jia, S. Mukerjee, R. Yang, Z. Jiang, D. Su, C. Liu and W. Xing, *ACS Catal.*, 2018, **8**, 2824–2832.
37 D. Malko, A. Kucernak and T. Lopes, *J. Am. Chem. Soc.*, 2016, **138**, 16056–16068.
38 D. Malko, A. Kucernak and T. Lopes, *Nat. Commun.*, 2016, **7**, 13285.
39 F. Xiao, Y. C. Wang, Z. P. Wu, G. Chen, F. Yang, S. Zhu, K. Siddharth, Z. Kong, A. Lu and J. C. Li, *Adv. Mater.*, 2021, **33**, 2006292.
40 L. Wang, X. Wan, S. Liu, L. Xu and J. Shui, *J. Energy Chem.*, 2019, **39**, 77–87.
41 T. Gao, Z. Zhu, Y. Li, H. Hu, H. Rong, W. Liu, T. Yang and X. Zhang, *Carbon*, 2021, **177**, 44–51.
42 D. Prendergast and G. Galli, *Phys. Rev. Lett.*, 2006, **96**, 215502.
43 B. Ravel and M. Newville, *J. Synchrotron Radiat.*, 2005, **12**, 537–541.
44 H. Yang, Y. Liu, X. Liu, X. Wang, H. Tian, G. I. N. Waterhouse, P. E. Kruger, S. G. Telfer and S. Ma, *eScience*, 2022, **2**, 227–234.
45 H. Zhang, Y. Wang, T. Wu, J. Yu, S. R. B. Arulmani, W. Chen, L. Huang, M. Su, J. Yan and X. Liu, *J. Alloys Compd.*, 2023, **944**, 169039.
46 L. Jiao, J. Li, L. L. Richard, Q. Sun, T. Stracensky, E. Liu, M. T. Sougrati, Z. Zhao, F. Yang, S. Zhong, H. Xu, S. Mukerjee, Y. Huang, D. A. Cullen, J. H. Park, M. Ferrandon, D. J. Myers, F. Jaouen and Q. Jia, *Nat. Mater.*, 2021, **20**, 1385–1391.
47 M. Mazzucato and C. Durante, *Electrochim. Acta*, 2023, **463**, 142801.
48 M. Primbs, Y. Sun, A. Roy, D. Malko, A. Mehmood, M.-T. Sougrati, P.-Y. Blanchard, G. Granozzi, T. Kosmala, G. Daniel, P. Atanassov, J. Sharman, C. Durante, A. Kucernak, D. Jones, F. Jaouen and P. Strasser, *Energy Environ. Sci.*, 2020, **13**, 2480–2500.
49 J.-C. Li, X. Qin, P.-X. Hou, M. Cheng, C. Shi, C. Liu, H.-M. Cheng and M. Shao, *Carbon*, 2019, **147**, 303–311.